nanomaterials

MDPI

Article

Quantum Spin Hall Effect in Two-Monolayer-Thick InN/InGaN Coupled Multiple Quantum Wells

Sławomir P. Łepkowski

Institute of High Pressure Physics—Unipress, Polish Academy of Sciences, ul. Sokołowska 29/37, 01-142 Warszawa, Poland; slawomir.lepkowski@unipress.waw.pl; Tel.: +48-510-332-238

Abstract: In this study, we present a theoretical study of the quantum spin Hall effect in InN/InGaN coupled multiple quantum wells with the individual well widths equal to two atomic monolayers. We consider triple and quadruple quantum wells in which the In content in the interwell barriers is greater than or equal to the In content in the external barriers. To calculate the electronic subbands in these nanostructures, we use the eight-band **k·p** Hamiltonian, assuming that the effective spin–orbit interaction in InN is negative, which represents the worst-case scenario for achieving a two-dimensional topological insulator. For triple quantum wells, we find that when the In contents of the external and interwell barriers are the same and the widths of the internal barriers are equal to two monolayers, a topological insulator with a bulk energy gap of 0.25 meV can appear. Increasing the In content in the interwell barriers leads to a significant increase in the bulk energy gap of the topological insulator, reaching about 0.8 meV. In these structures, the topological insulator can be achieved when the In content in the external barriers is about 0.64, causing relatively low strain in quantum wells and making the epitaxial growth of these structures within the range of current technology. Using the effective 2D Hamiltonian, we study the edge states in strip structures containing topological triple quantum wells. We demonstrate that the opening of the gap in the spectrum of the edge states caused by decreasing the width of the strip has an oscillatory character regardless of whether the pseudospin-mixing elements of the effective Hamiltonian are omitted or taken into account. The strength of the finite size effect in these structures is several times smaller than that in HgTe/HgCdTe and InAs/GaSb/AlSb topological insulators. Therefore, its influence on the quantum spin Hall effect is negligible in strips with a width larger than 150 nm, unless the temperature at which electron transport is measured is less than 1 mK. In the case of quadruple quantum wells, we find the topological insulator phase only when the In content in the interwell barriers is larger than in the external barriers. We show that in these structures, a topological insulator with a bulk energy gap of 0.038 meV can be achieved when the In content in the external barriers is about 0.75. Since this value of the bulk energy gap is very small, quadruple quantum wells are less useful for realizing a measurable quantum spin Hall system, but they are still attractive for achieving a topological phase transition and a nonlocal topological semimetal phase.

Keywords: quantum spin Hall effect; topological insulators; group-III nitrides; coupled quantum wells

Citation: Łepkowski, S.P. Quantum Spin Hall Effect in Two-Monolayer-Thick InN/InGaN Coupled Multiple Quantum Wells. *Nanomaterials* **2023**, *13*, 2212. https://doi.org/10.3390/nano13152212

Academic Editors: Filippo Giannazzo and Yia-Chung Chang

Received: 16 June 2023
Revised: 18 July 2023
Accepted: 27 July 2023
Published: 30 July 2023

1. Introduction

The quantum spin Hall effect (QSHE) occurring in 2D topological insulators (TIs) is characterized by gapless helical edge states inside the bulk 2D subband spectrum [1,2]. These edge states are counter-propagating Kramers partners, so backscattering is suppressed and ballistic transport can occur, making 2D TIs interesting candidates for many applications in spintronics and low-power electronics [3–7]. Two-dimensional TIs can also host Majorana bound states when combined with superconductors, which makes them promising materials for topological quantum computing [8–12]. The QSHE was initially predicted for graphene, where the spin–orbit interaction (SOI) produces gaps with opposite

signs at the K and K′ points of the hexagonal Brillouin zone [13]. Recently, it has been experimentally confirmed that graphene is a 2D TI with a very small value of the bulk energy gap, E_{2Dg}^{TI}, equal to 0.042 meV [14]. A QSHE with much larger values of E_{2Dg}^{TI} than that in graphene was discovered in HgTe/CdTe and InAs/GaSb/AlSb quantum wells (QWs) [15–18]. In HgTe/CdTe QWs, the QSHE arises from the strong SOI in the HgTe layers, which inverts the subband structure when the QW width exceeds a critical value for the topological phase transition (TPT), i.e., $L_{qw}^{TI} = 6.4$ nm [15,16]. For HgTe/CdTe QWs typically grown on CdTe substrates, E_{2Dg}^{TI} reaches about 15 meV and it can be significantly increased up to 55 meV when virtual substrates, introducing compressive stress, are used [19]. In InAs/GaSb two-layer QWs, embedded between AlSb barriers, the TI phase originates from the fact that the valence band (VB) in GaSb is higher than the conduction band (CB) in InAs and the inverted subbands can be obtained by varying the widths of the InAs and GaSb layers [17,18]. In these structures, E_{2Dg}^{TI} is of the order of a few meV and it can be increased to up to 35 meV by adding In to GaSb in InAs/GaInSb QWs [20,21]. A further increase in E_{2Dg}^{TI} to 45 meV was achieved by adding an additional InAs layer to InAs/GaInSb QWs and an E_{2Dg}^{TI} value of 60 meV was theoretically predicted for these three-layer InAs/GaInSb/InAs QWs [22,23].

Two-dimensional TIs have also been proposed theoretically for InN/GaN, InGaN/GaN, and InN/InGaN QWs grown along the [0001] direction [24–26]. For these structures, the large built-in electric field originating from the piezoelectric effect and spontaneous polarization may invert the ordering of the CB and VB subbands according to the quantum confined Stark effect (QCSE). This phenomenon, called the polarization-induced TPT, was initially proposed for InN/GaN QWs with L_{qw}^{TI} equal to four atomic monolayers (MLs) [24]. The predicted values of E_{2Dg}^{TI} in these structures depend significantly on the assumed intrinsic SOI in InN, which is still under scientific debate [26–29]. It was found that E_{2Dg}^{TI} can reach 5 meV when a positive SOI of the order of a few meV is assumed in InN, or it can be about 1.25 meV when a negative SOI in InN is considered [24–26]. The disadvantage of InN/GaN QWs is their very large strain of 11%, which dramatically complicates the growth of these structures. In $In_xGa_{1-x}N$/GaN and InN/$In_yGa_{1-y}N$ QWs, strain can be significantly reduced by decreasing the lattice misfit between the materials of barriers and wells. However, decreasing strain causes a reduction in the built-in electric field, which consequently leads to an increase in L_{qw}^{TI} [24,26]. In $In_xGa_{1-x}N$/GaN QWs, L_{qw}^{TI} increases faster with decreasing In content in the QWs than the critical thickness for the pseudomorphic growth [24,26]. The situation is more promising in InN/$In_yGa_{1-y}N$ QWs, where L_{qw}^{TI} increases slower with increasing In content in the barriers, y, than the critical thickness for the pseudomorphic growth [26]. For InN/$In_yGa_{1-y}N$ QWs with the In content $y = 0.316$ and $L_{qw}^{TI} = 1.8$ nm, E_{2Dg}^{TI} can reach about 2 meV, assuming a negative SOI in InN [26]. Increasing the In content y leads to an increase in L_{qw}^{TI} and a decrease in E_{2Dg}^{TI} [26]. For InN/$In_yGa_{1-y}N$ QWs with the In content $y = 0.79$ and $L_{qw}^{TI} = 4$ nm, a TI state with $E_{2Dg}^{TI} = 0.52$ meV was predicted [26].

The TI phase in InGaN-based QWs has not yet been confirmed experimentally due to problems with the growth of topological structures with an inverted order of the CB and VB subbands. The difficulties of growing $In_xGa_{1-x}N$/GaN QWs with an In content higher than 0.25 were known almost from the beginning of nitride-based optoelectronics, and for many years they were the main obstacles to obtaining light-emitting diodes and lasers operating in the green and red spectral regions [30,31]. It was realized that the reason for these problems is the existence of biaxial strain in $In_xGa_{1-x}N$ layers, which hinders the incorporation of In atoms in the $In_xGa_{1-x}N$ lattice due to the so-called compositional pulling effect [30,31]. Strain was also found to be the main limitation in the growth of ML-thick InN/GaN superlattices [32–38]. Structures with nominal InN MLs grown on GaN showed much shorter light emission wavelengths, indicating $In_xGa_{1-x}N$ alloys instead of InN [32–35]. Measurements performed using high-resolution transmission electron microscopy revealed that ultra-thin nominal InN layers are always some form of $In_xGa_{1-x}N$ alloy with the

In content smaller than 0.35 [35–38]. Theoretical calculations show a tendency towards ordering in $In_xGa_{1-x}N$ epitaxial layers caused by local strain effects [39–41]. For growth under N-rich conditions, the upper limit of the In content is equal to 0.25 due to repulsive In–In strain interactions, which cause a steep increase in the chemical potential [40,41]. For growth under metal-rich conditions, the chemical potential exhibits a significant nonlinear increase when the In content exceeds 0.33 [41]. Recently, the latter compositional limit has been surpassed in the case of one-ML-thick $In_xGa_{1-x}N/GaN$ QWs with an In content of approximately 0.45 [42]. A further increase in the In incorporation in $In_xGa_{1-x}N$ QWs can be achieved by using metamorphic $In_xGa_{1-x}N$ buffers or InGaN pseudo-substrates, which reduce biaxial compressive strain in these structures [41,43–47]. Much less effort has been devoted to developing the growth of $InN/In_yGa_{1-y}N$ QWs. In the literature, there are only a few papers that report on the growth of $InN/In_yGa_{1-y}N$ QWs [48–50]. In these structures, the In content y is between 0.8 and 0.9, and the QW widths are equal to 3 and 4.5 nm. It is worth noting that 4.5 nm wide $InN/In_{0.8}Ga_{0.2}N$ QWs could be close to the TPT, as shown in [26]. However, photoluminescence measurements performed on $InN/In_yGa_{1-y}N$ QWs showed that the energy gap (E_{2Dg}) was about 0.7 eV, suggesting a rather weak contribution from the QCSE [48–50]. The weak QCSE in the structures presented in [48–50] can originate from screening of the built-in electric field by free carriers created by unintentional doping. Another reason is the use of relatively small barrier widths in [48–50], which resulted in a decrease in the built-in electric field in the QWs and an increase in the built-in electric field in the barriers [26].

The possibility of increasing the strength of the QCSE without changing the strain in the system and the thickness of QWs can be achieved in coupled double QWs (DQWs) with thin interwell barriers. This effect was clearly demonstrated by comparing the optical properties of a single $In_xGa_{1-x}N/GaN$ QW with DQWs having the same compositions and widths of individual wells [51]. It was shown that the recombination energy of interwell indirect excitons in $In_{0.17}Ga_{0.83}N/GaN$ DQWs with individual QW widths of 2.6 nm is about 350 meV smaller than the recombination energy of excitons in a single QW with the same In content and a thickness of 2.6 nm [51]. This idea of increasing the strength of the QCSE has recently been used in theoretical calculations predicting the TPT in $In_xGa_{1-x}N/GaN$ and $InN/In_yGa_{1-y}N$ DQWs [52]. It was shown that the TI phase can be achieved in these structures when the interwell barrier is sufficiently thin and the widths of individual QWs are 2 and 3 MLs, or 3 and 3 MLs [52]. For $InN/In_yGa_{1-y}N$ DQWs with $L_{qw}^{TI} = 3$ MLs, E_{2Dg}^{TI} can reach about 1.2 meV when the negative SOI in InN is taken into account [52]. However, the In content y that is required to achieve the TI phase in these structures is about 0.33 [52], which is far from the values reached so far in the growth of $InN/In_yGa_{1-y}N$ QWs [48–50].

In this work, we extend the study of the TI phase to coupled InN-based triple and quadruple QWs in which the In content in the interwell barriers, z, is greater than or equal to the In content in the external barriers, y (see Figure 1). We denote these structures as $InN/In_zGa_{1-z}N/In_yGa_{1-y}N$ multiple QWs. We consider only structures in which the widths of individual QWs are equal to 2 MLs. We use the eight-band **k·p** method, assuming that the SOI in InN is negative, which represents the worst-case scenario for achieving the TI phase in these nanostructures. We first investigate triple quantum wells (TQWs) with the same In contents z and y. We show that a TI state with an E_{2Dg}^{TI} of 0.25 meV can appear in TQWs when the widths of interwell barriers (L_{ib}) are equal to 2 MLs, whereas for structures with L_{ib} = 3 MLs, the TI phase does not occur. Then, we study TQWs in which the In content z in the interwell barriers is greater than the In content y in the external barriers. We find that increasing the In content z leads to a significant increase in E_{2Dg}^{TI} to about 0.8 meV. In these TQWs, the TI phase can be achieved when the In content y is about 0.64, causing relatively low strain in QWs and making the epitaxial growth of these structures in the range of current technology [42,49]. Next, we generate the effective 2D Hamiltonian and study the QSHE in strip structures containing $InN/In_zGa_{1-z}N/In_yGa_{1-y}N$ TQWs. By reducing the width of the strip from 200 to 50 nm, we observe the opening of a gap in the

spectrum of the edge states, which is known as the finite size effect and originates from the interaction between the edge states on opposite sides of the strip [53–55]. We demonstrate that the finite size effect in InN/In$_z$Ga$_{1-z}$N/In$_y$Ga$_{1-y}$N TQWs has an oscillatory character regardless of whether the pseudospin-mixing elements of the effective Hamiltonian are omitted or taken into account. We also reveal that the strength of the finite size effect in InN/In$_z$Ga$_{1-z}$N/In$_y$Ga$_{1-y}$N TQWs is several times smaller than in HgTe/HgCdTe and InAs/GaSb/AlSb QWs; therefore, its influence on the QSHE is negligible in strips wider than 150 nm. In the case of InN/In$_z$Ga$_{1-z}$N/In$_y$Ga$_{1-y}$N quadruple quantum wells (QQWs), we find that the TI phase appears only when z > y. We show that in these structures, a TI phase with $E_{2Dg}^{TI} = 0.038$ meV can be reached when the In content y is about 0.75. Since the values of E_{2Dg}^{TI} in QQWs are very small, these structures are less useful for realizing a measurable quantum spin Hall system, but are still attractive for achieving the TPT.

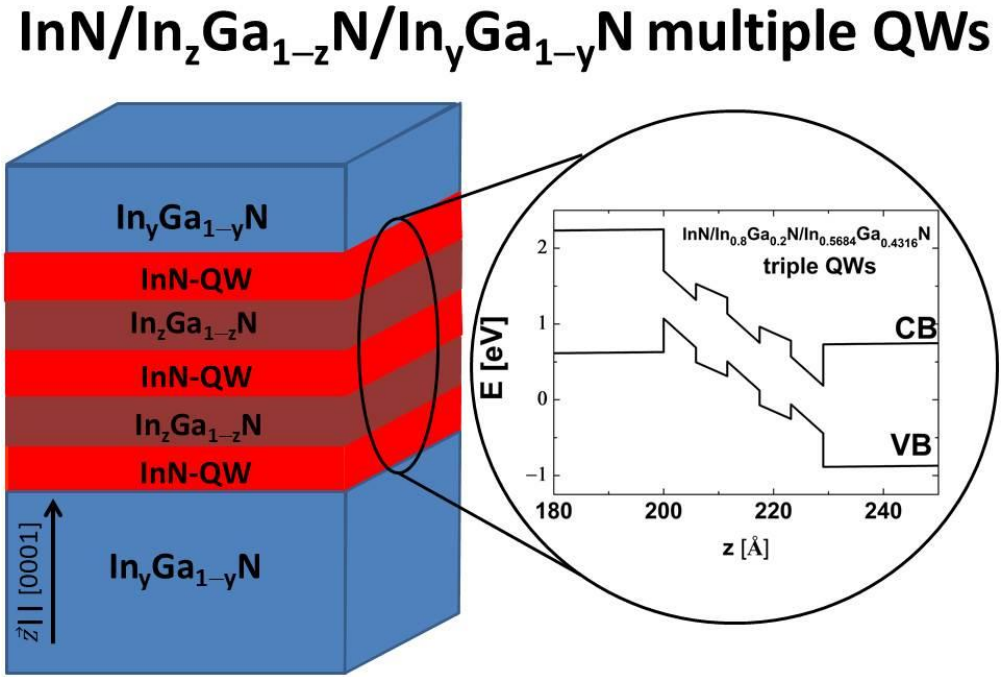

Figure 1. Schematic representation of InN/In$_z$Ga$_{1-z}$N/In$_y$Ga$_{1-y}$N coupled multiple QWs. The right-hand side shows the CB and VB edge profiles for an exemplary structure containing InN/In$_{0.8}$Ga$_{0.2}$N/In$_{0.5684}$Ga$_{0.4316}$N triple QWs with the widths of individual QWs and interwell barriers equal to 2 MLs.

2. Theoretical Model

We consider InN/In$_z$Ga$_{1-z}$N/In$_y$Ga$_{1-y}$N coupled multiple QWs that are grown on virtual substrates having the same In content as external In$_y$Ga$_{1-y}$N barriers (see Figure 1). We assume that the thickness of external barriers is large (2000 nm), since this makes the built-in electric field in the QWs extremely large, so the TI phase is easier to achieve [26,52]. For simplicity, we assume that the chemical compositions of interwell barriers are identical. The individual QWs and the interwell barriers are ultra-thin layers, whose widths are expressed in MLs. An ML of InGaN is a double layer of In (Ga) and N atoms, the thickness of which is equal to half of the *c* lattice constant [24]. Therefore, the width of a QW (L_{qw}) and the width of an interwell barrier (L_{ib}) can be expressed by the following formula:

$$L_l = \frac{1}{2} n_l c_l (1 - R_{B,l}\varepsilon_{xx,l}),\ l = qw,\ ib \tag{1}$$

where n_l is the number of MLs in the layer, c_l denotes the *c*-lattice constant of unstrained material of the layer, $R_{B,l}$ is the biaxial relaxation coefficient, $\varepsilon_{xx,l} = \frac{a_s}{a_l} - 1$ is the in-plane

strain, and a_l and a_s are the a-lattice constants of unstrained materials of the layer and the substrate, respectively. We took the lattice constants for InN and GaN from [56] and assumed that for InGaN alloys, they depend linearly on composition [57]. The R_B coefficient is given as follows:

$$R_B = \frac{1}{\varepsilon_{xx}}\left[1 - \sqrt{1 + \frac{2}{C_{333}}\left(-c + \sqrt{c^2 - 2C_{333}d}\right)}\right] \tag{2}$$

where $c = C_{33} + 2C_{133}\left(\varepsilon_{xx} + \frac{1}{2}\varepsilon_{xx}^2\right)$ and $d = 2C_{13}\left(\varepsilon_{xx} + \frac{1}{2}\varepsilon_{xx}^2\right) + (C_{113} + C_{123})\left(\varepsilon_{xx} + \frac{1}{2}\varepsilon_{xx}^2\right)^2$ [58–60]. In the above formula, C_{13} and C_{33} are the second-order elastic constants, while C_{113}, C_{123}, C_{133}, and C_{333} are the third-order elastic constants [60]. We took the elastic constants for GaN and InN from [60], while for InGaN alloys, we assumed linear dependences on composition for the third-order elastic constants and took the nonlinear composition dependences of the second-order elastic constants from [61,62]. The built-in electric field in the multiple QW structure is calculated taking into account the first- and second-order piezoelectric effects and the spontaneous polarization [63,64]. We assume that the structures are undoped, so screening of the built-in electric field by free carriers is not considered.

In order to calculate the electronic states in $InN/In_zGa_{1-z}N/In_yGa_{1-y}N$ multiple QWs, we apply the $\mathbf{k}\cdot\mathbf{p}$ method with the 8-band Hamiltonian $H^{8\times8}$, which includes relativistic and nonrelativistic linear-wave-vector terms [26,28]. This Hamiltonian takes into account the negative SOI in InN, which was predicted via ab initio calculations performed using the quasiparticle self-consistent GW method [26,28]. For the bulk 3D crystals, the Hamiltonian $H^{8\times8}$ has the following form:

$$H^{8\times8} = \begin{bmatrix} H_c & -Q & Q^* & R & 0 & 0 & 0 & 0 \\ -Q^* & F & K^* & M_-^* & 0 & 0 & -W^* & 0 \\ Q & K & G & -N_+ & 0 & -W^* & -T & \sqrt{2}\Delta_3 \\ R & M_- & -N_+^* & L & 0 & 0 & \sqrt{2}\Delta_3 & -S^* \\ 0 & 0 & 0 & 0 & H_c & Q^* & -Q & R \\ 0 & 0 & -W & 0 & Q & F & K & -M_+ \\ 0 & -W & -T^* & \sqrt{2}\Delta_3 & -Q^* & K^* & G & N_-^* \\ 0 & 0 & \sqrt{2}\Delta_3 & -S & R & -M_+^* & N_- & L \end{bmatrix} \begin{matrix} |iS,\uparrow\rangle \\ |-(X+iY)/\sqrt{2},\uparrow\rangle \\ |(X-iY)/\sqrt{2},\uparrow\rangle \\ |Z,\uparrow\rangle \\ |iS,\downarrow\rangle \\ |(X-iY)/\sqrt{2},\downarrow\rangle \\ |-(X+iY)/\sqrt{2},\downarrow\rangle \\ |Z,\downarrow\rangle \end{matrix} \tag{3}$$

where $H_c = E_{vb} + E_g + A_{c\perp}k_\perp^2 + A_{c||}k_z^2$, $Q = P_2k_+/\sqrt{2}$, $R = P_1k_z$, $F = \Delta_1 + \Delta_2 + (A_2 + A_4)k_\perp^2 + (A_1 + A_3)k_z^2$, $G = F - 2\Delta_2$, $L = A_2k_\perp^2 + A_1k_z^2$, $K = A_5k_+^2$, $M_+ = [A_6k_z + i(A_7 + \alpha_4)]k_+$, $M_- = [A_6k_z - i(A_7 + \alpha_4)]k_+$, $N_+ = [A_6k_z + i(A_7 - \alpha_4)]k_+$, $N_- = [A_6k_z - i(A_7 - \alpha_4)]k_+$, $S = i\alpha_1k_+$, $T = i\alpha_2k_+$, and $W = i(\alpha_1 + \alpha_3)k_+$. The top valence band energy and the energy gap are denoted by E_{vb} and E_g, respectively. $A_{c\perp}$ and $A_{c||}$ describe the dispersion of the CB, whereas P_1 and P_2 are the Kane parameters [25,26]. The valence band parameters $A_1, \ldots, A_7$, $\alpha_1, \ldots, \alpha_4$, and $\Delta_1, \ldots, \Delta_3$ were taken from [28] assuming linear dependences on composition in InGaN alloys. Additionally, the parameters $A_1, \ldots, A_6$ were rescaled according to [25]. Strain and the built-in electric field were included in the Hamiltonian $H^{8\times8}$ according to [65,66]. Since for QWs grown along the [0001] crystallographic direction, k_z is not a good quantum number, we replaced it with the operator $-i\frac{\partial}{\partial z}$. The standard symmetrization of operators containing the product of functions and derivatives was used to ensure the Hermiticity of $H^{8\times8}\left(\vec{k}_\perp, k_z = -i\frac{\partial}{\partial z}\right)$ [25]. The subband dispersion in $InN/In_zGa_{1-z}N/In_yGa_{1-y}N$ multiple QWs is obtained by numerically solving the eigenvalue problem with the Hamiltonian $H^{8\times8}\left(\vec{k}_\perp, k_z = -i\frac{\partial}{\partial z}\right)$ [26,67].

To check the applicability of the 8-band **k·p** method to determine the TPT in 2ML-thick InGaN-based coupled multiple QWs, we performed calculations of the energy gap (E_g) in short-period $In_xGa_{1-x}N/GaN$ superlattices (SLs) and compared the results to those obtained via ab initio calculations [68,69] and photoluminescence measurements [70]. We chose SLs with the widths of QWs and barriers equal to 2 MLs and we assumed that the structures were grown pseudomorphically on GaN substrates. Periodic boundary conditions for the wavefunctions were used in the calculations of the E_g in SLs [71]. In Figure 2, we compare the E_g obtained using the Hamiltonian $H^{8\times8}$ (a solid line) with the ab initio results (squares) and experimental data (dot) taken from [68–70]. One can see that the **k·p** method determines the E_g well for $In_{0.33}Ga_{0.67}N/GaN$ SLs. For larger In contents, the **k·p** method slightly overestimates the values of E_g compared to the ab initio calculations. In general, however, a satisfactory agreement between these two approaches is reached.

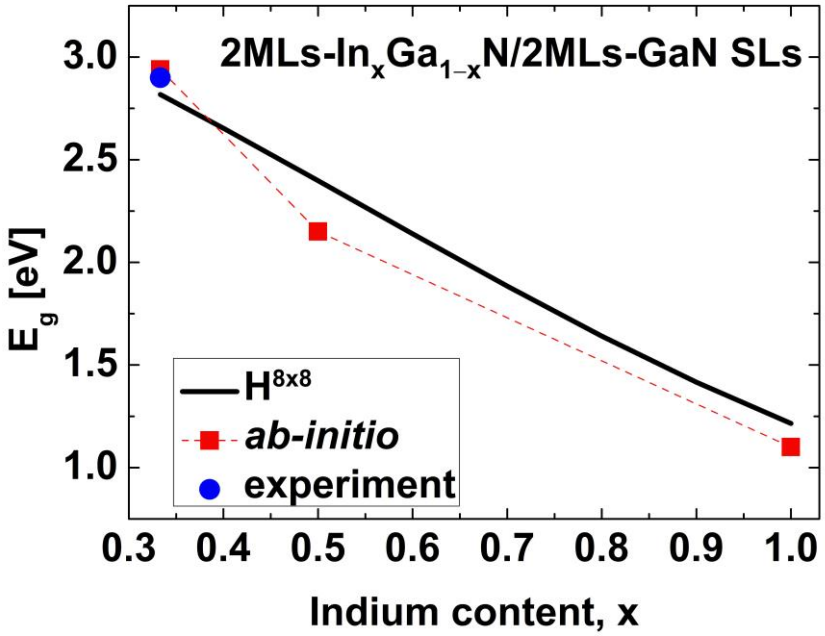

Figure 2. E_g for 2 MLs-$In_xGa_{1-x}N$/2MLs-GaN SLs as a function of the In content x. The solid line corresponds to the results obtained using the 8-band **k·p** method, while squares and the dot represent the results of ab initio calculations and photoluminescence measurements taken from [68–70].

In order to calculate the electronic states in a strip of finite width, we apply the effective 2D Hamiltonian H_{eff}, which describes the subband dispersion near the energy gap [25,26]. The basis of the Hamiltonian H_{eff} consists of six eigenstates corresponding to three doubly degenerate levels of the Hamiltonian $H^{8\times8}\left(\vec{k}_\perp = 0,\ k_z = -i\frac{\partial}{\partial z}\right)$, i.e., the lowest CB level and the highest light-hole (LH) and heavy-hole (HH) levels. These states have well-defined projections of the total angular momentum onto the z axis equal to $\pm\frac{1}{2}$ for the CB and LH states and $\pm\frac{3}{2}$ for the HH states. The Hamiltonian H_{eff} has the following form:

$$H_{eff} = \begin{array}{c} \begin{matrix} |CB,1/2\rangle & |LH,-1/2\rangle & |HH,3/2\rangle & |CB,-1/2\rangle & |LH,1/2\rangle & |HH,-3/2\rangle \end{matrix} \\ \begin{bmatrix} E_0+E_1k_\perp^2 & C_2k_- & C_1k_+ & iC_3k_- & iMk_\perp^2 & iB_2k_-^2 \\ C_2k_+ & L_0+L_1k_\perp^2 & B_1k_+^2 & -iMk_\perp^2 & iC_4k_+ & iC_5k_- \\ C_1k_- & B_1k_-^2 & H_0+H_1k_\perp^2 & -iB_2k_-^2 & iC_5k_- & 0 \\ -iC_3k_+ & iMk_\perp^2 & iB_2k_+^2 & E_0+E_1k_\perp^2 & -C_2k_+ & -C_1k_- \\ -iMk_\perp^2 & -iC_4k_- & -iC_5k_+ & -C_2k_- & L_0+L_1k_\perp^2 & B_1k_-^2 \\ -iB_2k_+^2 & -iC_5k_+ & 0 & -C_1k_+ & B_1k_+^2 & H_0+H_1k_\perp^2 \end{bmatrix} \end{array} \quad (4)$$

where E_0, L_0, and H_0 are the energies of the states $|CB,\pm1/2\rangle$, $|LH,\pm1/2\rangle$, and $|HH,\pm1/2\rangle$, respectively. The coefficients B_1, C_1, and C_2 determine the coupling between states with

the same pseudospins, whereas the coefficients B_2, C_3, C_4, C_5, and M describe the coupling between states with the opposite pseudospins [25]. The coupling between states with different pseudospins is due to the structural asymmetry of the QW potential, which originates from the built-in electric field (see Figure 1) [25]. All of the coefficients of the Hamiltonian H_{eff} are obtained by applying the mini-band **k·p** method and the Löwdin perturbation approach [25,26]. We assume that the strip is oriented along the x axis, so k_y is not a good quantum number and we replace it with the operator $-i\frac{\partial}{\partial y}$. The dispersion of electronic states in a strip is obtained by numerically solving the eigenvalue problem with the Hamiltonian $H_{eff}\left(k_x,\ k_y = -i\frac{\partial}{\partial y}\right)$ [26,67].

3. Results and Discussion

As we mentioned in the introduction, we investigated the QSHE effect in InN/$In_zGa_{1-z}N$/$In_yGa_{1-y}N$ TQWs and QQWs in which the In content in the internal barriers, z, was greater than or equal to the In content in the external barriers, y. The widths of individual QWs were equal to 2 MLs. We first studied InN/$In_zGa_{1-z}N$/$In_yGa_{1-y}N$ TQWs with z = y. We considered two types of structures with L_{ib} equal to 2 MLs (2–2–2–2–2) and 3 MLs (2–3–2–3–2). In Figure 3, we present E_{2Dg} as a function of the In content y and the subband dispersions for distinct phases occurring in these structures. For the structures with L_{ib} = 2 MLs, we observe that a decrease in the In content y causes TPT from the normal insulator (NI) to the TI phase via the Weyl semimetal (WSM) phase. For the NI phase, the CB subband is above the LH subband; for the WSM phase, both subbands touch at finite $\vec{k}_{\perp}$; for the TI phase, the LH subband is above the CB subband. TPT occurs in the structure with the In content $y_{TPT} = 0.30675$. In the TI phase, E_{2Dg}^{TI} reaches a maximum value of $E_{2Dg,max}^{TI} = 0.255$ meV at the In content $y_{TI,max} = 0.3058$. For this structure, the amplitude of the built-in electric field in QWs $|F_{qw}|$ is equal to 10.87 MV/cm. For an In content y smaller than $y_{NTSM} = 0.3036$, we obtain a nonlocal topological semimetal (NTSM), arising from nonlocal overlapping between the LH and CB subbands [25,26]. For structures with L_{ib} = 3MLs, the TI phase does not occur. In these structures, we find that reducing the In content y below 0.3029 causes a non-topological phase transition from the NI phase to the nonlocal nontopological semimetal (NNSM), characterized by normal ordering of the CB and LH subbands [52]. Further decreasing y results in a TPT from the NNSM to the NTSM via the buried Weyl semimetal (BWSM) phase [52]. The phase transitions described above are similar to the phase transitions found in InN/$In_yGa_{1-y}N$ DQWs [52]. In particular, for very similar In contents in the barriers, the TI phase appeared in InN/$In_yGa_{1-y}N$ DQWs with L_{qw} = 3 MLs [52]. The obvious advantage of InN/$In_zGa_{1-z}N$/$In_yGa_{1-y}N$ TQWs over InN/$In_yGa_{1-y}N$ DQWs is that in the former case, the TI occurs at L_{qw} = 2 MLs. However, a significant disadvantage of InN/$In_yGa_{1-y}N$/$In_yGa_{1-y}N$ TQWs is a much smaller $E_{2Dg,max}^{TI}$ compared to InN/$In_yGa_{1-y}N$ DQWs, for which a value of about 1.2 meV was reached [52].

To increase E_{2Dg}^{TI} in TQWs, we propose to use InN/$In_zGa_{1-z}N$/$In_yGa_{1-y}N$ TQWs in which z > y. We focus on structures with L_{ib} = 2 MLs. In Figure 4, we show E_{2Dg} as a function of the In content y for structures with an In content z equal to 0.5, 0.6, 0.7, 0.8, and 0.9. In all of these cases, we find the TI phase between the WSM and the NTSM. For the InN/$In_{0.5}Ga_{0.5}N$/$In_yGa_{1-y}N$ TQWs (Figure 4a), $E_{2Dg,max}^{TI}$ is equal to 0.523 meV, which is twice as large as the $E_{2Dg,max}^{TI}$ obtained for InN/$In_zGa_{1-z}N$/$In_yGa_{1-y}N$ TQWs with z = y. $E_{2Dg,max}^{TI}$ increases with increasing the In content z from 0.5 to 0.8, reaching the largest value equal to 0.832 meV for InN/$In_{0.8}Ga_{0.2}N$/$In_yGa_{1-y}N$ TQWs (see Figure 4d). For InN/$In_{0.9}Ga_{0.1}N$/$In_yGa_{1-y}N$ TQWs, we find that $E_{2Dg,max}^{TI}$ is equal to 0.796 meV. The obtained values of $E_{2Dg,max}^{TI}$ are large enough to allow experimental verification of the QSHE in TQWs [14,72]. The values of y_{TPT} and $y_{TI,max}$ increase monotonically with increasing z. We note that for InN/$In_{0.9}Ga_{0.1}N$/$In_yGa_{1-y}N$ TQWs, $y_{TI,max}$ reaches 0.6345, causing a relatively low strain in the QW layers of about 0.0367 and making the epitaxial growth of these structures within the range of current technology [42,49]. The properties of the TI

phase in InN/In$_z$Ga$_{1-z}$N/In$_y$Ga$_{1-y}$N TQWs are presented overall in Figure 5. Figure 5a shows that y_{TPT} and the amplitude of strain in the QWs at the TPT, $\left|\varepsilon_{xx,qw}^{TPT}\right|$, depend almost linearly on z. In Figure 5b, we demonstrate the values of $E_{2Dg,max}^{TI}$ and the window of the In content for the TI phase, $\Delta y_{TI} = y_{TPT} - y_{NTSM}$, as a function of z. We can see that both of these quantities depend non-monotonically on z. For smaller values of z, the increases in $E_{2Dg,max}^{TI}$ and Δy_{TI} are related to the increase in the difference between the LH and HH energy levels at $\vec{k}_{\perp} = 0$ (denoted by ΔE_{LH-HH}) and to the decrease in the amplitude of the built-in electric field in QWs $|F_{qw}|$, as shown in Figure 5c. We note that the decrease in $|F_{qw}|$ increases the overlap of the wavefunctions of the CB and LH states due to the QCSE, reducing the tendency for nonlocal overlapping between the CB and LH subbands. For z = 0.9, the reductions in $E_{2Dg,max}^{TI}$ and Δy_{TI} are associated with smaller quantum confinement and leakage of the CB wavefunction into the external barrier, which decreases the overlap between the wavefunctions of the CB and LH states and increases the nonlocal overlapping between the CB and LH subbands.

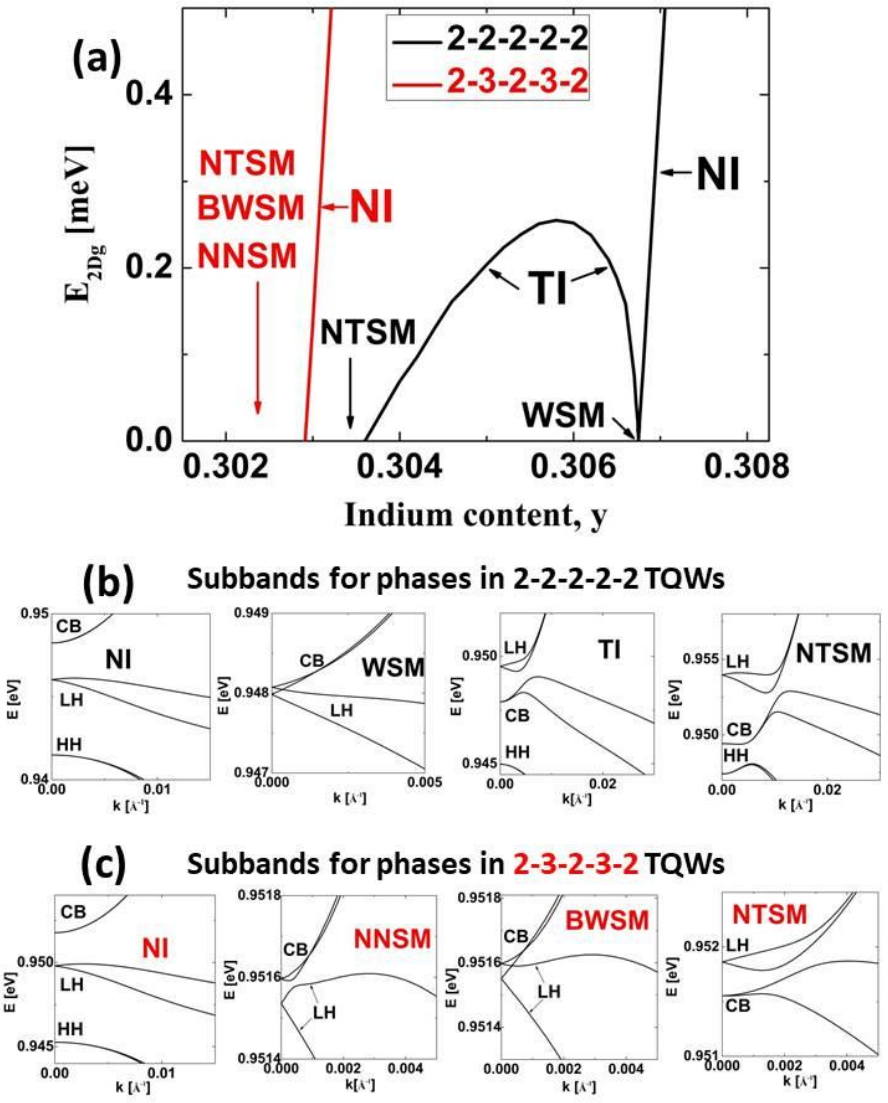

Figure 3. (**a**) E_{2Dg} for InN/In$_z$Ga$_{1-z}$N/In$_y$Ga$_{1-y}$N TQWs with z = y as a function of the In content y. The widths of individual QWs are equal to 2MLs and the widths of interwell barriers are equal to 2 MLs (2–2–2–2–2) and 3 MLs (2–3–2–3–2). (**b**,**c**) Subband dispersions for the phases in 2–2–2–2–2 TQWs (**b**) and in 2–3–2–3–2 TQWs (**c**). The phases appear in order of decreasing In content in the barriers.

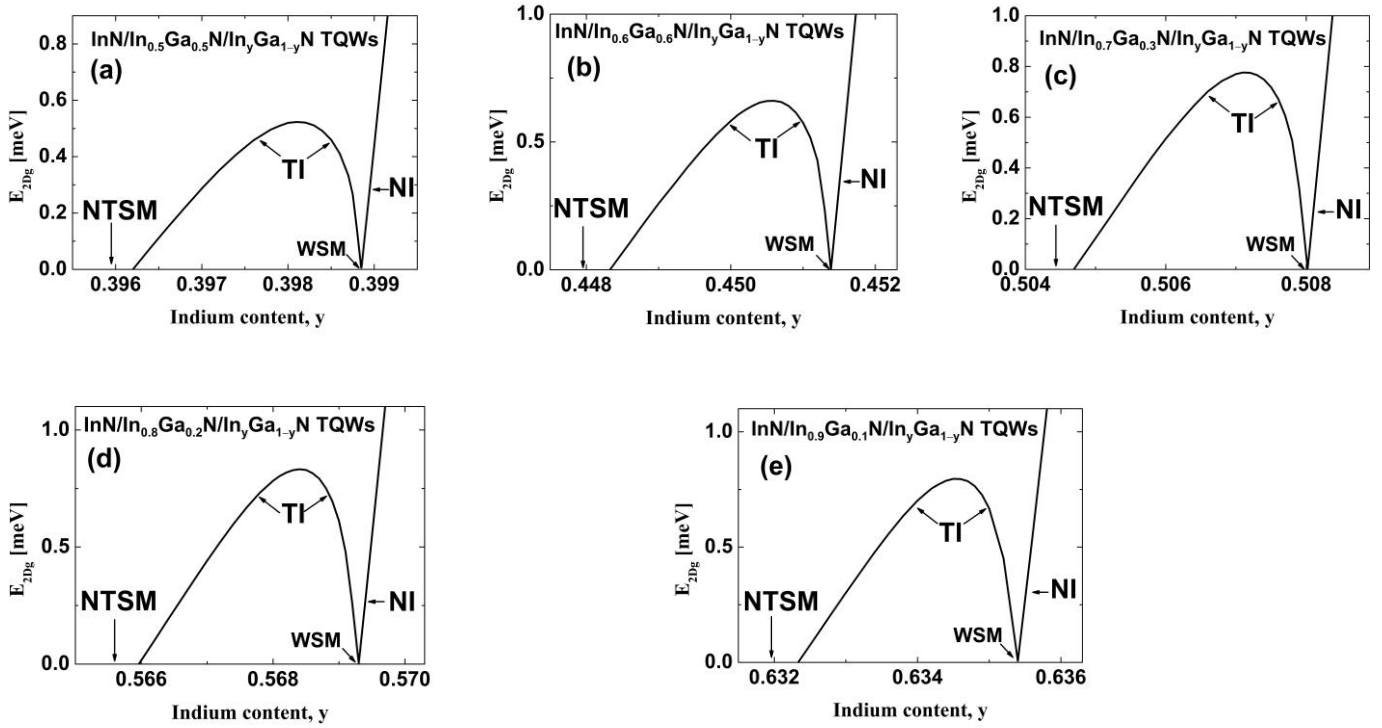

Figure 4. E_{2Dg} for $InN/In_zGa_{1-z}N/In_yGa_{1-y}N$ TQWs with different In content z in the interwell barriers equal to 0.5 (**a**), 0.6 (**b**), 0.7 (**c**), 0.8 (**d**), and 0.9 (**e**), as a function of the In content y in the external barriers. The widths of individual QWs and interwell barriers are equal to 2 MLs.

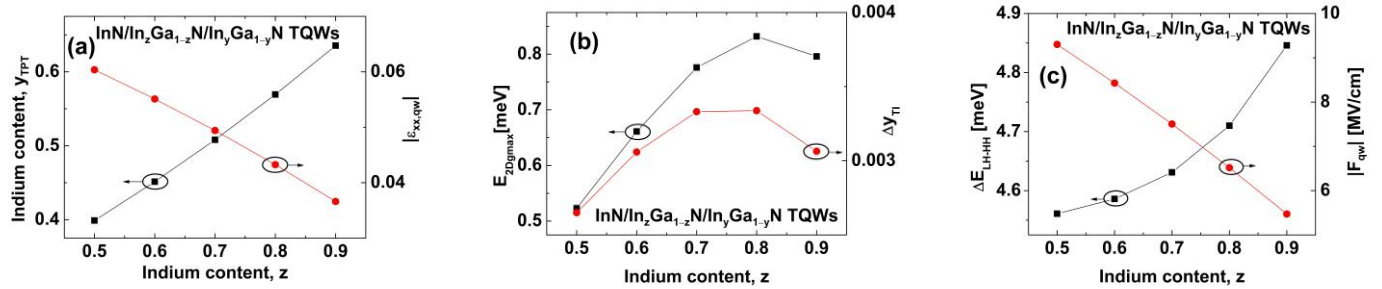

Figure 5. (**a**) Values of y_{TPT} (squares) and $\left|\varepsilon_{xx,qw}^{TPT}\right|$ (dots) for $InN/In_zGa_{1-z}N/In_yGa_{1-y}N$ TQWs as a function of the In content z. (**b**) Values of $E_{2Dg,max}^{TI}$ (squares) and Δy_{TI} (dots) for $InN/In_zGa_{1-z}N/In_yGa_{1-y}N$ TQWs as a function of the In content z. (**c**) Values of ΔE_{LH-HH} (squares) and $|F_{qw}|$ (dots) for $InN/In_zGa_{1-z}N/In_yGa_{1-y}N$ TQWs as a function of the In content z.

In order to study the QSHE occurring in the TI phase, we applied the effective 2D Hamiltonian H_{eff} and computed the electronic states in strip structures containing $InN/In_zGa_{1-z}N/In_yGa_{1-y}N$ TQWs. We chose the $InN/In_{0.8}Ga_{0.2}N/In_{0.5684}Ga_{0.4316}N$ TQWs for which we obtained the largest value of $E_{2Dg,max}^{TI}$. To determine the coefficients of the Hamiltonian H_{eff}, we used 150 states of the Hamiltonian $H^{8\times8}\left(\vec{k}_\perp = 0,\ k_z = -i\frac{\partial}{\partial z}\right)$; namely, 25 doubly degenerate states for the CB, LH, and HH subbands. We obtained the following values of the coefficients of the Hamiltonian H_{eff}: $E_0 = 0.745696$ eV, $L_0 = 0.748218$ eV, $H_0 = 0.743508$ eV, $E_1 = 3.525123$ eV·Å^2, $L_1 = -18.907530$ eV·Å^2, $H_1 = -18.825562$ eV·Å^2, $B_1 = 16.652953$ eV·Å^2, $C_1 = -0.189983$ eV·Å, $C_2 = 0.187564$ eV·Å, $B_2 = -0.849472$ eV·Å^2, $C_3 = 0.017855$ eV·Å, $C_4 = -0.068348$ eV·Å, $C_5 = -0.003012$ eV·Å, and $M = 1.152510$ eV·Å^2. The amplitudes of the linear (C_3, C_4, C_5) and quadratic (B_2, M) coefficients describing the coupling between states with the opposite pseudospins are sig-

nificantly smaller than the amplitudes of the linear (C_1, C_2) and quadratic (B_1) coefficients determining the coupling between states with the same pseudospins. The coefficients C_3, C_4, C_5, B_2, M were neglected in several papers on topological InN/GaN QWs [24,73,74], although they were found to play a key role in determining the TPT in these structures [25]. Below, we will show that they are important for determining the spectrum of the edge states in strip structures.

In Figure 6a, we compare the subband dispersions in InN/$In_{0.8}Ga_{0.2}$N/$In_{0.5684}Ga_{0.4316}$N TQWs obtained using the $\mathbf{k}\cdot\mathbf{p}$ Hamiltonian $H^{8\times8}$ (red lines) and the Hamiltonian H_{eff} (black lines). We can see that the Hamiltonian H_{eff} describes quite well the dispersions of the LH, CB, and HH subbands in the small vicinity of $\vec{k}_{\perp} = 0$, which is similar to the results obtained for HgTe/CdTe TQWs [75]. However, the Hamiltonian H_{eff} significantly overestimates E_{2Dg}^{TI}. Therefore, it is not suitable for studying the phase transitions in InN/In_zGa_{1-z}N/In_yGa_{1-y}N TQWs. Despite this disadvantage, it can be used to investigate edge states with small wavevectors, occurring in strips of finite thickness. In Figure 6b,c, we show the dispersion of electronic states in strips with widths L_{strip} of 200 nm and 50 nm. For a strip with $L_{strip} = 200$ nm, one can see that the Dirac point of the edge state dispersion curve is located in the bulk band gap. For a strip with $L_{strip} = 50$ nm, we observe a gap in the spectrum of the edge states (E_{edg}). The appearance of E_{edg} originates from the interaction between the edge states on opposite sides of the strip and is called the finite size effect [53–55]. Figure 6d demonstrates E_{edg} on a logarithmic scale as a function of L_{strip}. The solid symbols (in red) correspond to the results obtained using the full Hamiltonian H_{eff}, while the open symbols (in black) represent the results obtained by neglecting the pseudospin-mixing elements of the Hamiltonian H_{eff} (i.e., assuming $B_2 = C_3 = C_4 = C_5 = M = 0$). One can see that the finite size effect in InN/In_zGa_{1-z}N/In_yGa_{1-y}N TQWs has an oscillatory character regardless of whether the pseudospin-mixing elements of the effective Hamiltonian are omitted or taken into account. A similar situation was found for InAs/GaSb/AlSb QWs, for which, as in the case of InN-based QWs, there is rather small overlapping between the wavefunctions of the CB and VB subbands [55]. The period of oscillations of E_{edg} and their rate of decay depend significantly on the inclusion of the pseudospin-mixing elements of the Hamiltonian H_{eff}. We found that for strips with $L_{strip} \geq 150$ nm, E_{edg} is smaller than 8.62×10^{-5} meV, which corresponds to a characteristic temperature $T^* = E_{edg}/k_B$ that is smaller than 1 mK. Therefore, we state that when $L_{strip} \geq 150$ nm, the finite size effect is negligible and has no influence on the current flow along the edges unless the temperature at which the experiment is performed is less than 1 mK. In Figure 6e, we compare E_{edg} and E_{2Dg} on a linear scale as a function of L_{strip}. Note that a tenfold magnification of the values of E_{edg} has been used. One can see that E_{edg} is at least twenty times smaller than E_{2Dg}. For HgTe/HgCdTe and InAs/GaSb/AlSb QWs, E_{edg} is at least five and four times smaller than E_{2Dg} when $L_{strip} \geq 50$ nm [55]. Additionally, for HgTe/HgCdTe QWs, the condition that E_{edg} is less than 8.62×10^{-5} meV (i.e., $T^* \leq 1$ mK) is fulfilled when $L_{strip} \geq 600$ nm [54]. Therefore, we conclude that the strength of the finite size effect in InN/In_zGa_{1-z}N/In_yGa_{1-y}N TQWs is several times smaller than in HgTe/HgCdTe and InAs/GaSb/AlSb QWs.

Finally, we extended our study to InN/In_zGa_{1-z}N/In_yGa_{1-y}N QQWs. We considered only structures with the widths of individual QWs and interwell barriers equal to 2MLs. For QQWs with z = y, we found that the TI phase does not occur and the phase transitions are similar to the case of TQWs with $L_{ib} = 3$ MLs, as shown in Figure 3a,c. For QQWs with z > y, the TI phase can appear between the WSM and the NTSM, as for TQWs with $L_{ib} = 2$ MLs. In Figure 7a, E_{2Dg} for InN/$In_{0.9}Ga_{0.1}$N/In_yGa_{1-y}N QQWs is shown as a function of the In content y. We can see that for these structures, the TI occurs when y is about 0.753, which is very close to InN/$In_{0.8}Ga_{0.2}$N QWs grown using plasma-assisted molecular-beam epitaxy [49]. Unfortunately, we found that $E_{2Dg,max}^{TI} = 0.038$ meV, which is more than 20 times smaller than the value of $E_{2Dg,max}^{TI}$ obtained for InN/$In_{0.9}Ga_{0.1}$N/In_yGa_{1-y}N TQWs (see Figure 4e) and is also smaller than E_{2Dg}^{TI} in graphene [14]. Figure 7b shows

that y_{TPT} and $\left|\varepsilon_{xx,qw}^{TPT}\right|$ change linearly with increasing the In content z in InN/$In_zGa_{1-z}N$/$In_yGa_{1-y}N$ QQWs. Figure 7c demonstrates that $E_{2Dg,max}^{TI}$ and Δy_{TI} increase linearly with increasing z, which originates from the increase in ΔE_{LH-HH} and the decrease in $\left|F_{qw}\right|$ in these structures, as shown in Figure 7d. For InN/$In_zGa_{1-z}N$/$In_yGa_{1-y}N$ QQWs, $E_{2Dg,max}^{TI}$ and Δy_{TI} are very small; therefore, we do not consider these nanostructures as candidates for an experimental verification of the QSHE and the TI phase. However, InN/$In_zGa_{1-z}N$/$In_yGa_{1-y}N$ QQWs can be very useful for achieving the TPT and the NTSM phase due to large values of y_{TPT} and y_{NTSM}, in comparison to topological TQWs.

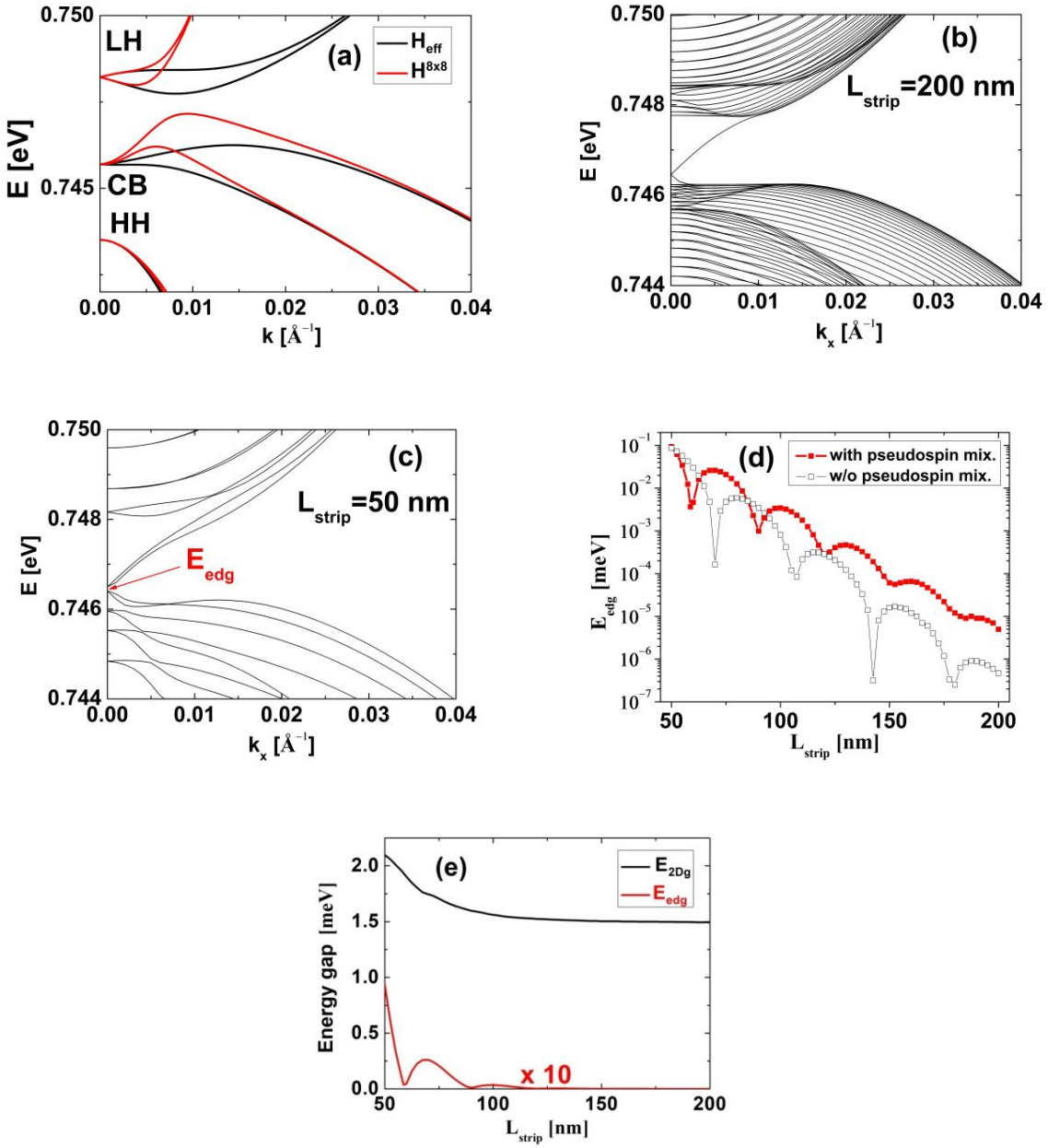

Figure 6. (**a**) Subband dispersions in topological InN/$In_{0.8}Ga_{0.2}N$/$In_{0.5684}Ga_{0.4316}N$ TQWs, obtained using the 8-band **k·p** Hamiltonian $H^{8\times8}$ (red lines) and the effective 2D Hamiltonian H_{eff} (black lines). (**b**,**c**) Dispersion of electronic states in strips containing InN/$In_{0.8}Ga_{0.2}N$/$In_{0.5684}Ga_{0.4316}N$ TQWs and having widths L_{strip} equal to 200 nm (**b**) and 50 nm (**c**). (**d**) E_{edg} (on a logarithmic scale) obtained with and w/o the pseudospin mixing elements of the Hamiltonian H_{eff} as a function of L_{strip}. (**e**) E_{edg} and E_{2Dg} (on a linear scale) as a function of L_{strip}. Note that the values of E_{edg} are magnified ten times.

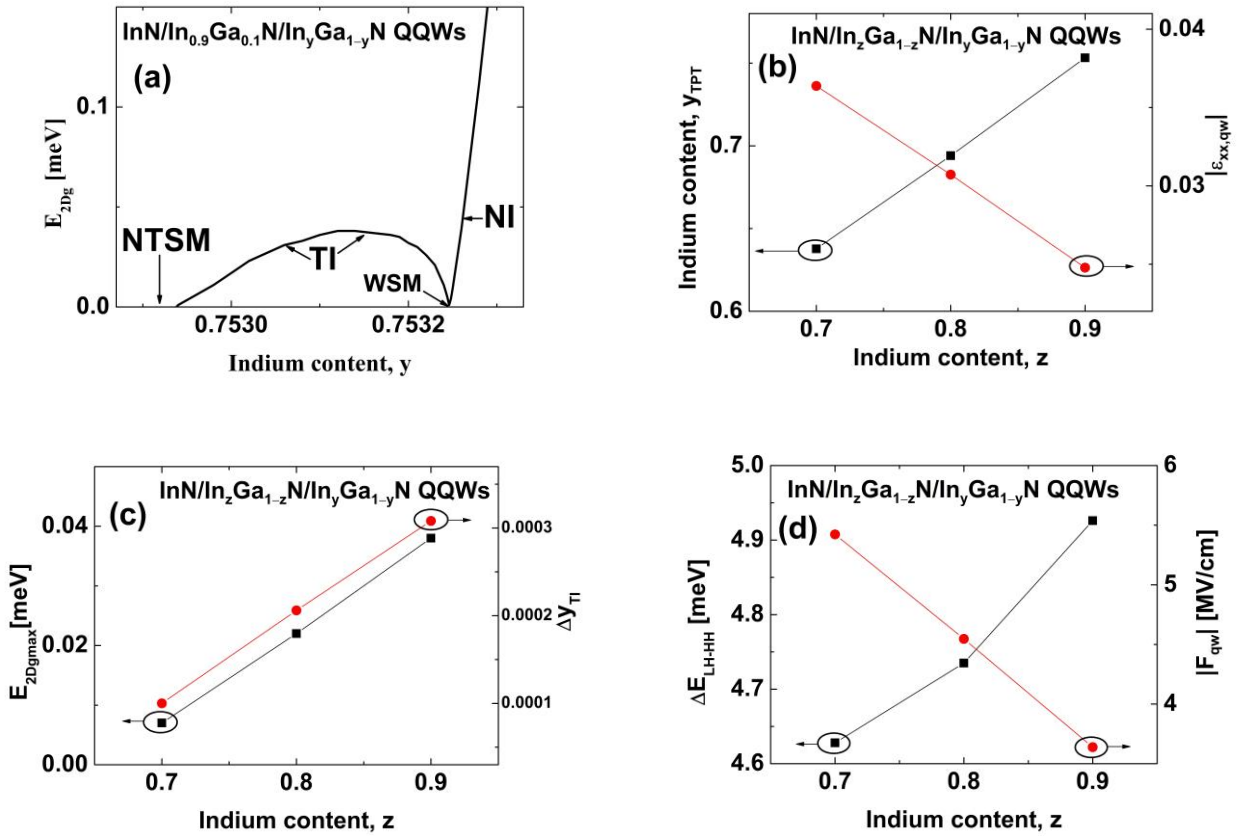

Figure 7. (**a**) E_{2Dg} for InN/$In_{0.9}Ga_{0.1}$N/In_yGa_{1-y}N QQWs as a function of the In content y. The widths of individual QWs and interwell barriers are equal to 2 MLs. (**b**) Values of y_{TPT} (squares) and $\left|\varepsilon_{xx,qw}^{TPT}\right|$ (dots) for InN/In_zGa_{1-z}N/In_yGa_{1-y}N QQWs as a function of the In content z. (**c**) Values of $E_{2Dg,max}^{TI}$ (squares) and Δy_{TI} (dots) for InN/In_zGa_{1-z}N/In_yGa_{1-y}N QQWs as a function of the In content z. (**d**) Values of ΔE_{LH-HH} (squares) and $\left|F_{qw}\right|$ (dots) for InN/In_zGa_{1-z}N/In_yGa_{1-y}N QQWs as a function of the In content z.

4. Conclusions

We have presented a theoretical proposal to obtain the TI phase and the QSHE in coupled InN/In_zGa_{1-z}N/In_yGa_{1-y}N TQWs with the widths of individual QWs and interwell barriers equal to 2 MLs. We have shown that for structures with the same In contents z and y, a TI state with an $E_{2Dg,max}^{TI}$ of 0.25 meV can appear. Increasing the In content z in TQWs with z > y leads to a significant increase in $E_{2Dg,max}^{TI}$ to about 0.8 meV. The TI phase in these structures can be achieved when the In content y is about 0.64, which results in relatively low strain in QWs and makes the epitaxial growth within the range of current technology [42,49]. We have demonstrated that the finite size effect in these structures has an oscillatory character regardless of whether the pseudospin-mixing elements of the effective Hamiltonian are omitted or taken into account. The strength of the finite size effect in InN/In_zGa_{1-z}N/In_yGa_{1-y}N TQWs is several times smaller than in HgTe/HgCdTe and InAs/GaSb/AlSb QWs; therefore, its influence on the QSHE is negligible in strips wider than 150 nm. In the case of InN/In_zGa_{1-z}N/In_yGa_{1-y}N QQWs, we found that the TI phase appears only when z > y. In these structures, the TI state with $E_{2Dg}^{TI} = 0.038$ meV can be reached when the In content y is about 0.75. Since the values of E_{2Dg}^{TI} in QQWs are very small, these structures are less useful for realizing a measurable quantum spin Hall system, but are still attractive for achieving the TPT and the NTSM. We hope that the presented results will guide future experimental studies to the discovery of the topological phases in group-III nitride nanostructures and contribute to new applications of these prospective topological nanomaterials.

Funding: This research received no external funding.

Data Availability Statement: The data underlying this article are available from the corresponding author on reasonable request.

Acknowledgments: The author would like to thank W. Bardyszewski from the Faculty of Physics, University of Warsaw, for suggesting he investigate the issue of topological insulators in triple InN/InGaN quantum wells.

Conflicts of Interest: The author declares no conflict of interest.

References

1. Hasan, M.Z.; Kane, C.L. Colloquium: Topological insulators. *Rev. Mod. Phys.* **2010**, *82*, 3045. [CrossRef]
2. Bansil, A.; Lin, H.; Das, T. Colloquium: Topological band theory. *Rev. Mod. Phys.* **2016**, *88*, 021004. [CrossRef]
3. Maciejko, J.; Hughes, T.L.; Zhang, S.C. The quantum spin Hall effect. *Annu. Rev. Condens. Matter Phys.* **2011**, *2*, 31–53. [CrossRef]
4. Hsu, C.H.; Stano, P.; Klinovaja, J.; Loss, D. Helical liquids in semiconductors. *Semicond. Sci. Technol.* **2021**, *36*, 123003. [CrossRef]
5. Yevtushenko, O.M.; Yudson, V. Protection of edge transport in quantum spin Hall samples: Spin-symmetry based general approach and examples. *New J. Phys.* **2022**, *24*, 023040. [CrossRef]
6. Dietl, T. Effects of charge dopants in quantum spin Hall materials. *Phys. Rev. Lett.* **2023**, *130*, 086202. [CrossRef]
7. Dietl, T. Quantitative theory of backscattering in topological HgTe and (Hg,Mn)Te quantum wells: Acceptor states, Kondo effect, precessional dephasing, and bound magnetic polaron. *Phys. Rev. B* **2023**, *107*, 085421. [CrossRef]
8. Nilsson, J.; Akhmerov, A.R.; Beenakker, C.W.J. Splitting of a cooper pair by a pair of Majorana bound states. *Phys. Rev. Lett.* **2008**, *101*, 120403. [CrossRef]
9. Elliot, S.R.; Franz, M. Colloquium: Majorana fermions in nuclear, particle, and solid-state physics. *Rev. Mod. Phys.* **2015**, *87*, 137. [CrossRef]
10. Li, J.; Pan, W.; Bernevig, B.A.; Lutchyn, R.M. Detection of Majorana Kramers pairs using a quantum point contact. *Phys. Rev. Lett.* **2016**, *117*, 046804. [CrossRef]
11. Aasen, D.; Hell, M.; Mishmash, R.V.; Higginbotham, A.; Danon, J.; Leijnse, M.; Jespersen, T.S.; Folk, J.A.; Marcus, C.M.; Flensberg, K.; et al. Milestones towards Majorana-based quantum computing. *Phys. Rev. X* **2016**, *6*, 031016. [CrossRef]
12. Schrade, C.; Fu, L. Quantum computing with Majorana Kramers pairs. *Phys. Rev. Lett.* **2022**, *129*, 227002. [CrossRef] [PubMed]
13. Kane, C.L.; Mele, E.J. Quantum spin Hall effect in graphene. *Phys. Rev. Lett.* **2005**, *95*, 226801. [CrossRef] [PubMed]
14. Sichau, J.; Prada, M.; Anlauf, T.; Lyon, T.J.; Bosnjak, B.; Tiemann, L.; Blick, R.H. Resonance microwave measurements of an intrinsic spin-orbit coupling gap in graphene: A possible indication of a topological state. *Phys. Rev. Lett.* **2019**, *122*, 046403. [CrossRef]
15. Bernevig, B.A.; Hughes, T.L.; Zhang, S.C. Quantum spin Hall effect and topological phase transition in HgTe quantum wells. *Science* **2006**, *314*, 1757–1761. [CrossRef]
16. Konig, M.; Wiedmann, S.; Brune, C.; Roth, A.; Buhmann, H.; Molenkamp, L.W.; Qi, X.L.; Zhang, S.C. Quantum spin Hall effect in HgTe quantum wells. *Science* **2007**, *318*, 766–770. [CrossRef]
17. Liu, C.; Hughes, T.L.; Qi, X.L.; Wang, K.; Zhang, S.C. Quantum spin Hall effect in inverted type-II semiconductors. *Phys. Rev. Lett.* **2008**, *100*, 236601. [CrossRef]
18. Knez, I.; Du, R.R.; Sullivan, G. Evidence for helical edge modes in inverted InAs/GaSb quantum wells. *Phys. Rev. Lett.* **2011**, *107*, 136603. [CrossRef]
19. Leubner, P.; Lunczer, L.; Brüne, C.; Buhmann, H.; Molenkamp, L.W. Strain engineering of the band gap of HgTe quantum wells using superlattice virtual substrates. *Phys. Rev. Lett.* **2016**, *117*, 086403. [CrossRef]
20. Du, L.; Li, T.; Lou, W.; Wu, X.; Liu, X.; Han, Z.; Zhang, C.; Sullivan, G.; Ikhlassi, A.; Chang, K.; et al. Tuning edge states in strained-layer InAs/GaInSb quantum spin Hall insulators. *Phys. Rev. Lett.* **2017**, *119*, 056803. [CrossRef]
21. Ire, H.; Akiho, T.; Couëdo, F.; Suzuki, K.; Onomitsu, K.; Muraki, K. Energy gap tuning and gate-controlled topological phase transition in InAs/$In_xGa_{1-x}Sb$ composite quantum wells. *Phys Rev. Mater.* **2020**, *4*, 104201. [CrossRef]
22. Avogadri, C.; Gebert, S.; Krishtopenko, S.S.; Castillo, I.; Consejo, C.; Ruffenach, S.; Roblin, C.; Bray, C.; Krupko, Y.; Juillaguet, S.; et al. Large inverted band gap in strained three-layer InAs/GaInSb quantum wells. *Phys. Rev. Res* **2022**, *4*, L042042. [CrossRef]
23. Krishtopenko, S.S.; Teppe, F. Quantum spin Hall insulator with a large bandgap, Dirac fermions, and bilayer graphene analog. *Sci. Adv.* **2022**, *4*, eaap7529. [CrossRef] [PubMed]
24. Miao, M.; Yan, Q.; Van de Walle, C.G.; Lou, W.K.; Li, L.L.; Chang, K. Polarization-driven topological insulator transition in a GaN/InN/GaN quantum well. *Phys. Rev. Lett.* **2012**, *109*, 186803. [CrossRef] [PubMed]
25. Łepkowski, S.P.; Bardyszewski, W. Topological phase transition and evolution of edge states in In-rich InGaN/GaN quantum wells under hydrostatic pressure. *J. Phys. Condens. Matter* **2017**, *29*, 055702. [CrossRef]
26. Łepkowski, S.P.; Bardyszewski, W. Topological insulator with negative spin-orbit coupling and transition between Weyl and Dirac semimetals in InGaN-based quantum wells. *Sci. Rep.* **2018**, *8*, 15403. [CrossRef]

27. de Carvalho, I.C.; Schleife, A.; Bechstedt, F. Influence of exchange and correlation on structural and electronic properties of AlN, GaN, and InN polytypes. *Phys. Rev. B* **2011**, *84*, 195105. [CrossRef]
28. Punya, A.; Lambrecht, W.R.L. Valence band effective-mass Hamiltonians for the group-III nitrides from quasiparticle self-consistent GW band structures. *Phys. Rev. B* **2012**, *85*, 195147. [CrossRef]
29. Lin, K.I.; Chen, Y.J.; Cheng, Y.C.; Gwo, S. Investigation of valence-band splitting in InN by low-temperature photoreflectance spectroscopy. *Jpn. J. Appl. Phys.* **2015**, *54*, 031001. [CrossRef]
30. Hiramatsu, K.; Kawaguchi, Y.; Shimizu, M.; Sawaki, N.; Zheleva, T.; Davis, R.F.; Tsuda, H.; Taki, W.; Kuwano, N.; Oki, K. The composition pulling effect in MOVPE grown InGaN on GaN and AlGaN and its TEM characterization. *MRS Internet J. Nitride Semicond.* **1997**, *2*, 6. [CrossRef]
31. Pereira, S.; Correia, M.R.; Pereira, E.; O'Donnell, K.P.; Trager-Cowan, C.; Sweeney, F.; Alves, E. Compositional pulling effects in $In_xGa_{1-x}N$/GaN layers: A combined depth-resolved cathodoluminescence and Rutherford backscattering/channeling study. *Phys. Rev. B* **2001**, *64*, 205311. [CrossRef]
32. Yoshikawa, A.; Che, S.B.; Yamaguchi, W.; Saito, H.; Wang, X.Q.; Ishitani, Y.; Hwang, E.S. Proposal and achievement of novel structure InN/GaN multiple quantum wells consisting of 1 ML and fractional monolayer InN wells inserted in GaN matrix. *Appl. Phys. Lett.* **2007**, *90*, 073101. [CrossRef]
33. Zhou, L.; Dimakis, E.; Hathwar, R.; Aoki, T.; Smith, D.J.; Moustakas, T.D.; Goodnick, S.M.; McCartney, M.R. Measurement and effects of polarization fields on one-monolayer-thick InN/GaN multiple quantum wells. *Phys. Rev. B* **2013**, *88*, 125310. [CrossRef]
34. Pan, W.; Dimakis, E.; Wang, G.T.; Moustakas, T.D.; Tsui, D.C. Two-dimensional electron gas in monolayer InN quantum wells. *Appl. Phys. Lett.* **2014**, *105*, 213503. [CrossRef]
35. Suski, T.; Schulz, T.; Albrecht, M.; Wang, X.Q.; Gorczyca, I.; Skrobas, K.; Christensen, E.; Svane, A. The discrepancies between theory and experiment in the optical emission of monolayer In(Ga)N quantum wells revisited by transmission electron microscopy. *Appl. Phys. Lett.* **2014**, *104*, 182103. [CrossRef]
36. Chèze, C.; Siekacz, M.; Isa, F.; Jenichen, B.; Feix, F.; Buller, J.; Schulz, T.; Albrecht, M.; Skierbiszewski, C.; Calarco, R.; et al. Investigation of interface abruptness and In content in (In,Ga)N/GaN superlattices. *J. Appl. Phys.* **2016**, *120*, 125307. [CrossRef]
37. Chèze, C.; Feix, F.; Riechert, H.; Brandt, O.; Calarco, R.; Anikeeva, M.; Schulz, T.; Albrecht, M. In/GaN(0001)-$(\sqrt{3} \times \sqrt{3})$ R30° adsorbate structure as a template for embedded (In,Ga)N/GaN monolayers and short-period superlattices. *Appl. Phys. Lett.* **2017**, *110*, 072104. [CrossRef]
38. Dimitrakopulos, G.P.; Vasileiadis, I.G.; Smalc-Koziorowska, J.; Kret, S.; Dimakis, E.; Florini, N.; Kehagias, T.; Suski, T.; Karakostas, T.; Moustakas, T.D.; et al. Compositional and strain analysis of In(Ga)N/GaN short period superlattices. *J. Appl. Phys.* **2018**, *123*, 024304. [CrossRef]
39. Lee, S.; Freysoldt, C.; Neugebauer, J. Ordering phenomena and formation of nanostructures in InxGa1-xN layers coherently grown on GaN(0001). *Phys. Rev. B* **2014**, *90*, 245301. [CrossRef]
40. Lymperakis, L.; Schulz, T.; Freysoldt, C.; Anikeeva, M.; Chen, Z.; Zheng, X.; Shen, B.; Chèze, C.; Siekacz, M.; Wang, X.Q.; et al. Elastically frustrated rehybridization: Origin of chemical order and compositional limits in InGaN quantum wells. *Phys. Rev. Mater.* **2018**, *2*, 011601. [CrossRef]
41. Schulz, T.; Lymperakis, L.; Anikeeva, M.; Siekacz, M.; Wolny, P.; Markurt, T.; Albrecht, M. Influence of strain on the indium incorporation in (0001) GaN. *Phys. Rev. Mater.* **2020**, *4*, 073404. [CrossRef]
42. Vasileiadis, I.G.; Lymperakis, L.; Adikimenakis, A.; Gkotinakos, A.; Devulapalli, V.; Liebscher, C.H.; Androulidaki, M.; Hubner, R.; Karakostas, T.; Georgakilas, A.; et al. Substitutional synthesis of sub-nanometer InGaN/GaN quantum wells with high indium content. *Sci. Rep.* **2021**, *11*, 20606. [CrossRef] [PubMed]
43. Sharma, T.K.; Towe, E. On ternary nitride substrates for visible semiconductor light-emitters. *Appl. Phys. Lett.* **2010**, *96*, 191105. [CrossRef]
44. Däubler, J.; Passow, T.; Aidam, R.; Köhler, K.; Kirste, L.; Kunzer, M.; Wagner, J. Long wavelength emitting GaInN quantum wells on metamorphic GaInN buffer layers with enlarged in-plane lattice parameter. *Appl. Phys. Lett.* **2014**, *105*, 111111. [CrossRef]
45. Fabien, C.A.M.; Gunning, B.P.; Doolittle, W.A.; Fischer, A.M.; Wei, Y.O.; Xie, H.; Ponce, F.A. Low-temperature growth of InGaN films over the entire composition range by MBE. *J. Cryst. Growth* **2015**, *425*, 115–118. [CrossRef]
46. Even, A.; Laval, G.; Ledoux, O.; Ferret, P.; Sotta, D.; Guiot, E.; Levy, F.; Robin, I.C.; Dussaigne, A. Enhanced In incorporation in full InGaN heterostructure grown on relaxed InGaN pseudo-substrate. *Appl. Phys. Lett.* **2017**, *110*, 262103. [CrossRef]
47. Pasayat, S.S.; Gupta, C.; Wong M., S.; Wang, Y.; Nakamura, S.; Denbaars S., P.; Keller, S.; Mishra U., K. Growth of strain-relaxed InGaN on micrometer-sized patterned compliant GaN pseudo-substrates. *Appl. Phys. Lett.* **2020**, *116*, 111101. [CrossRef]
48. Grandal, J.; Pereiro, J.; Bengoechea-Encabo, A.; Fernández-Garrido, S.; Sánchez-Garcia, M.A.; Munoz, E.; Calleja, E.; Luna, E.; Trampert, A. InN/InGaN multiple quantum wells emitting at 1.5 μm grown by molecular beam epitaxy. *Appl. Phys. Lett.* **2011**, *98*, 061901. [CrossRef]
49. Naranjo, F.B.; Kandaswamy, P.K.; Valdueza-Felip, S.; Calvo, V.; González-Herráez, M.; Martin-López, S.; Corredera, P.; Méndez, J.A.; Mutta, G.R.; Lacroix, B.; et al. Nonlinear absorption of InN/InGaN multiple-quantum well structures at optical telecommunication wavelengths. *Appl. Phys. Lett.* **2011**, *98*, 031902. [CrossRef]
50. Valdueza-Felip, S.; Rigutti, L.; Naranjo, F.B.; Ruterana, P.; Mangeney, J.; Julien, F.H.; González-Herráez, M.; Monroy, E. Carrier localization in InN/InGaN multiple-quantum wells with high In-content. *Appl. Phys. Lett.* **2012**, *101*, 062109. [CrossRef]

51. Suski, T.; Staszczak, G.; Korona, K.P.; Lefebvre, P.; Monroy, E.; Drozdz, P.A.; Muzioł, G.; Skierbiszewski, C.; Kulczykowski, M.; Matuszewski, M.; et al. Switching of exciton character in double InGaN/GaN quantum wells. *Phys. Rev. B* **2018**, *98*, 165302. [CrossRef]
52. Łepkowski, S.P.; Anwar, A.R. Polarization-induced phase transitions in ultra-thin InGaN-based double quantum wells. *Nanomaterials* **2022**, *12*, 2418. [CrossRef]
53. Zhou, B.; Lu, H.Z.; Chu, R.L.; Shen, S.Q.; Niu, Q. Finite size effects on helical edge states in a quantum spin-Hall system. *Phys. Rev. Lett.* **2008**, *101*, 246807. [CrossRef] [PubMed]
54. Zhi, C.; Bin, Z. Finite size effects on helical edge states in HgTe quantum wells with the spin-orbit coupling due to bulk- and structure-inversion asymmetries. *Chin. Phys. B* **2014**, *23*, 037304. [CrossRef]
55. Papaj, M.; Cywiński, Ł.; Wróbel, J.; Dietl, T. Conductance oscillations in quantum point contacts of InAs/GaSb heterostructures. *Phys. Rev. B* **2016**, *93*, 195305. [CrossRef]
56. Vurgaftman, I.; Meyer, J.R. Band parameters for nitrogen-containing semiconductors. *J. Appl. Phys.* **2003**, *94*, 3675. [CrossRef]
57. Gorczyca, I.; Łepkowski, S.P.; Suski, T.; Christensen, N.E.; Svane, A. Influence of indium clustering on the band structure of semiconducting ternary and quaternary nitride alloys. *Phys. Rev. B* **2009**, *80*, 075202. [CrossRef]
58. Łepkowski, S.P.; Bardyszewski, W. Anomalous Rashba spin-orbit interaction in electrically controlled topological insulator based on InN/GaN quantum wells. *J. Phys. Condens. Matter* **2017**, *29*, 195702. [CrossRef] [PubMed]
59. Łepkowski, S.P.; Bardyszewski, W. Corrigendum: Anomalous Rashba spin-orbit interaction in electrically controlled topological insulator based on InN/GaN quantum wells (2017 J. Phys.: Condens. Matter 29, 195702). *J. Phys. Condens. Matter* **2020**, *33*, 119501. [CrossRef]
60. Łepkowski, S.P.; Anwar, A.R. Third-order elastic constants and biaxial relaxation coefficient in wurtzite group-III nitrides by hybrid-density functional theory calculations. *J. Phys. Condens. Matter* **2021**, *33*, 355402. [CrossRef]
61. Łepkowski, S.P.; Anwar, A.R. Biaxial relaxation coefficient in group-III nitride quantum wells and thin films. *Acta Phys. Pol. A* **2022**, *141*, 130–134. [CrossRef]
62. Łepkowski, S.P. Inapplicability of Martin transformation to elastic constants of zinc-blende and wurtzite group-III nitride alloys. *J. Appl. Phys.* **2015**, *117*, 105703. [CrossRef]
63. Bernardini, F.; Fiorentini, V. Spontaneous versus piezoelectric polarization in III-V nitrides: Conceptual aspects and practical consequences. *Phys. Stat. Sol.* **1999**, *216*, 391–398. [CrossRef]
64. Prodhomme, P.-Y.; Beya-Wakata, A.; Bester, G. Nonlinear piezoelectricity in wurtzite semiconductors. *Phys. Rev. B* **2013**, *88*, 121304. [CrossRef]
65. Chuang, S.L.; Chang, C.S. k·p method for strained wurtzite semiconductors. *Phys. Rev. B* **1996**, *54*, 2491–2504. [CrossRef]
66. Łepkowski, S.P.; Gorczyca, I.; Stefańska-Skrobas, K.; Christensen, N.E.; Svane, A. Deformation potentials in AlGaN and InGaN alloys and their impact on optical polarization properties of nitride quantum wells. *Phys. Rev. B* **2013**, *88*, 081202. [CrossRef]
67. Huebner, K.H.; Thornton, E.A. *The Finite Element Method for Engineers*; Wiley: New York, NY, USA, 1982.
68. Gorczyca, I.; Suski, T.; Strak, P.; Staszczak, G.; Christensen, N.E. Band gap engineering of In(Ga)N/GaN short period superlattices. *Sci. Rep.* **2017**, *7*, 16055. [CrossRef]
69. Gorczyca, I.; Suski, T.; Christensen, N.E.; Svane, A. Theoretical study of nitride short period superlattices. *J. Phys. Condens. Matter* **2018**, *30*. [CrossRef] [PubMed]
70. Staszczak, G.; Gorczyca, I.; Grzanka, E.; Smalc-Koziorowska, J.; Targowski, G.; Czernecki, R.; Siekacz, M.; Grzanka, S.; Skierbiszewski, C.; Schulz, T.; et al. Bandgap behavior of InGaN/GaN short period superlattices grown by metal-organic vapor phase epitaxy. *Phys. Stat. Sol.* **2017**, *254*, 1600710. [CrossRef]
71. Nakamura, K.; Shimizu, A.; Koshiba, M.; Hayata, K. Finite-element analysis of the miniband structures of semiconductor superlattices with arbitrary periodic potential profiles. *IEEE J. Quantum Electron.* **1991**, *27*, 2035–2041. [CrossRef]
72. Olshanetsky, E.B.; Kvon, Z.D.; Gusev, G.M.; Levin, A.D.; Raichev, O.E.; Mikhailov, N.N.; Dvoretsky, S.A. Persistence of a two-dimensional topological insulator state in wide HgTe quantum wells. *Phys. Rev. Lett.* **2015**, *114*, 126802. [CrossRef] [PubMed]
73. Dan, M.; Hu, G.; Li, I.; Zhang, Y. High performance piezotronic logic nanodevices based on GaN/InN/GaN topological insulator. *Nano Energy* **2018**, *50*, 544–551. [CrossRef]
74. Litvinov, V.I. Quantum anomalous Hall state with Chern number C = 2 in wurtzite quantum wells. *Phys. Rev. B* **2021**, *104*, 245304. [CrossRef]
75. Ferreira, G.J.; Candido, D.R.; Hernandez, F.G.G.; Gusev, G.M.; Olshanetsky, E.B.; Mikhailov, N.N.; Dvoretsky, S.A. Engineering topological phases in triple HgTe/CdTe quantum wells. *Sci. Rep.* **2022**, *12*, 2617. [CrossRef] [PubMed]